Radiative Viscous-Shock-Layer Solutions with Coupled Ablation Injection

James N. Moss*
NASA Langley Research Center, Hampton, Va.

This paper describes a viscous-shock-layer analysis for investigating high energy equilibrium flowfields about blunt axisymmetric bodies. The analysis includes radiation transfer, mass injection, diffusion, and visous effects. Radiation transfer is calculated with a nongray radiation model that accounts for line and continuum radiation. The analysis can treat large levels of blowing for both stagnation and downstream flow. Results are presented for selected Earth entry conditions that demonstrate the essential features of this analysis. Particular emphasis is given to the effects of mass injection on stagnation and downstream flow. Results for both specified and coupled ablation injection are presented.

Nomenclature

C_A = ablator mass fraction
C_i = mass fraction of species i, ρ_i/ρ
$\tilde{C}_l$ = mass fraction of element l
C_p = frozen specific heat of mixture, $\sum_i C_i C_{p,i}$
$C_{p,i}$ = specific heat of species i, $C^*_{p,i}/C^*_{p,\infty}$
D_{ij} = binary diffusion coefficients
h = enthalpy of mixture, $\sum_i C_i h_i$
h_i = enthalpy of species, i, h^*_i/U^{*2}_∞
H = total enthalpy of mixture (Eq. 7), H^*/U^{*2}_∞
K = thermal conductivity of mixture, $K^*/\mu^*(T^*_{\text{ref}})C^*_{p,\infty}$
$\dot{m}$ = mass injection rate, $\dot{m}^*/\rho^*_\infty U^*_\infty$
M^*_i = molecular weight of species i
$\bar{M}^*$ = molecular weight of mixture
n = coordinate measured normal to the body, n^*/R^*_N
N_{Pr} = Prandtl number, $N_{Pr}=\mu^* C^*_p/K^*$
N_{Le} = Lewis number, $N_{Le}=\rho^* D^*_{ij} C^*_p/K^*$
N_{Sc} = Schmidt number, $N_{Sc}=N_{Pr}/N_{Le}$
p = pressure, $p^*/(\rho^*_\infty U^{*2}_\infty)$
q_r = net radiant heat flux in n-direction, $q^*_r/\rho^*_\infty U^{*3}_\infty$
$q_r{}^{(+)*}$ = component of radiant flux away from wall
$q_r{}^{(-)*}$ = component of radiant flux toward the wall
$-q_{c,w}$ = convective heat flux toward the wall (Eq. 14)
Q = divergence of the net radiant heat flux, $Q^* R^*_N/\rho^*_\infty U^{*3}_\infty$
r = radius measured from axis of symmetry to a point on the body surface, r^*/R^*_N
R^* = universal gas constant
R^*_N = nose radius
s = coordinate measured along the body surface, s^*/R^*_N
T = temperature, T^*/T^*_{ref}
T^*_{ref} = reference temperature, $U^{*2}_\infty/C^*_{p\infty}$
u = velocity component tangent to body surface, u^*/U^*_∞
U^*_∞ = freestream velocity
v = velocity component normal to body surface, v^*/U^*_∞
α = shock angle defined in Fig. 1
δ_{il} = number of atoms of the lth element in species i
ΔH^*_a = heat of ablation
ϵ = Reynolds number parameter (Eq. 7) and char emissivity (Eq. 13)
θ = body angle defined in Fig. 1
η = transformed n coordinate, n/n_s
κ = body curvature, $\kappa^* R^*_N$
μ = viscosity of mixture, μ^*/μ^*_{ref}
μ^*_{ref} = reference viscosity, $\mu^*(T^*_{\text{ref}})$
ξ = coordinate measured along the body surface, $\xi = s$
ρ = density of mixture, ρ^*/ρ^*_∞
σ^* = Stefan Boltzmann constant

Subscripts

i = ith species
l = lth element
s = shock value
w = wall value
∞ = freestream condition
$-$ = values for the solid ablation material at the surface
υ = radiation frequency

Superscripts

j = zero for plane flow and one for axisymmetric flow
$-$ = quantity divided by its corresponding shock value
$*$ = dimensional quantity
$'$ = total differential

Introduction

SEVERAL analyses[1-7] have been developed for studying stagnation or near-stagnation viscous flows about planetary probes. This flowfield problem is complex due to mass injection into the flow and radiative transport. To provide an adequate design capability for planetary probes, it is essential that downstream as well as stagnation analyses exist. This is particularly true for the high-energy flowfield because no experimental data exists from tests in which the thermodynamic environment of planetary entries is fully duplicated. Furthermore, the interaction of the flowfield with the thermal-protection material can result in moderate to massive ablation injection rates, depending on the planetary mission. Consequently, a need exists for high-energy viscous flowfield analyses with the capability of calculating stagnation and downstream flows for any injection rate.

Sutton[8] and Chou[9] have recently presented stagnation and downstream solutions for viscous radiating flows. Sutton's analysis is a direct method that involves coupling a boundary-layer solution with an inviscid shock-layer solution. That analysis has been applied to problems with zero-to-moderate mass injection. Chou's analysis accounts for massive blowing, but is an indirect method where the equations are solved by a locally nonsimilar approach.

In this study, a viscous-shock-layer analysis is presented and applied to high-energy equilibrium flows about blunt

Presented as Paper 74-73 at the AIAA 12th Aerospace Sciences Meeting, Washington, D. C., Jan. 30-Feb. 1, 1974; submitted April 15, 1975; revision received December 22, 1975.

Index category: Radiatively Coupled Flows and Heat Transfer.

*Research Scientist. Member AIAA.

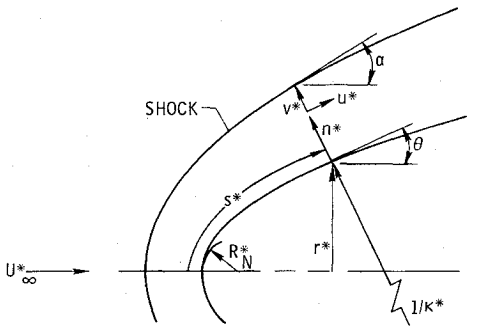

Fig. 1 Coordinate system.

axisymmetric bodies at zero angle of attack. This analysis, based on the analysis developed by Davis[10] for a perfect gas, includes mass injection, radiation transfer, diffusion, and viscous effects. The analysis is direct and provides both stagnation and downstream solution for large levels of blowing. Radiation transfer is calculated with a nongray radiation model that accounts for line and continuum radiation. Results are presented for Earth entry conditions to demonstrate the essential features of this analysis. Particular emphasis is given to the effects of mass injection on the stagnation and downstream flow. Results for both specified and coupled mass injection are present. The injectants considered are the species for air, a carbon-phenolic ablator, and a phenolic-nylon ablator. This is the first direct analysis that provides nonsimilar downstream solutions for radiative viscous flows for large blowing.

Analysis

Governing Equations

The viscous-shock-layer equations are obtained from the steady-state Navier-Stokes equations by keeping terms up to second-order in the inverse square root of the Reynolds No. ϵ.[10] Consequently, one set of equations is solved for both the inviscid and viscous regions. The viscous-shock-layer equations for an equilibrium multicomponent gas mixture are developed in Refs. 11 and 12. The same viscous-shock-layer equations are solved in the present study with the addition of radiation transport for a blunted axisymmetric body at zero angle of attack. The body-oriented coordinate system is shown in Fig. 1. With the assumption of binary diffusion, the nondimensional equations are

Global continuity

$$\frac{\partial}{\partial s}[(r+n\cos\theta)^j \rho u] + \frac{\partial}{\partial n}[(1+n\kappa)(r+n\cos\theta)^j \rho v] = 0 \qquad (1)$$

s-momentum

$$\rho\left(\frac{u}{1+n\kappa}\frac{\partial u}{\partial s} + v\frac{\partial u}{\partial n} + \frac{uv\kappa}{1+n\kappa}\right) + \frac{1}{1+n\kappa}\frac{\partial p}{\partial s} = \epsilon^2\left\{\frac{\partial}{\partial n}\left[\mu\left(\frac{\partial u}{\partial n} - \frac{u\kappa}{1+n\kappa}\right)\right] + \mu\left(\frac{2\kappa}{1+n\kappa} + \frac{j\cos\theta}{r+n\cos\theta}\right)\times\left(\frac{\partial u}{\partial n} - \frac{u\kappa}{1+n\kappa}\right)\right\} \qquad (2)$$

n-momentum

$$\rho\left(\frac{u}{1+n\kappa}\frac{\partial v}{\partial s} + v\frac{\partial v}{\partial n} - \frac{u^2\kappa}{1+n\kappa}\right) + \frac{\partial p}{\partial n} = 0 \qquad (3a)$$

where the thin shock-layer forms of Eq. (3a) is

$$\frac{\partial p}{\partial n} = \frac{\rho u^2 \kappa}{1+n\kappa} \qquad (3b)$$

Energy

$$\rho\left(\frac{u}{1+n\kappa}\frac{\partial H}{\partial s} + v\frac{\partial H}{\partial n}\right) - v\frac{\partial p}{\partial n} + \frac{\rho\kappa u^2 v}{1+n\kappa} = \epsilon^2\left[\frac{\partial \Phi}{\partial n} + \Phi\left(\frac{\kappa}{1+n\kappa} + \frac{j\cos\theta}{r+n\cos\theta}\right)\right] - Q \qquad (4)$$

Elemental continuity

$$\rho\left(\frac{u}{1+n\kappa}\frac{\partial \tilde{C}_l}{\partial s} + v\frac{\partial \tilde{C}_l}{\partial n}\right) = \frac{\epsilon^2}{(1+n\kappa)(r+n\cos\theta)^j} \times\left\{\frac{\partial}{\partial n}\left[(1+n\kappa)(r+n\cos\theta)^j \frac{\mu}{N_{Sc}}\frac{\partial \tilde{C}_l}{\partial n}\right]\right) \qquad (5)$$

State

$$p = \rho T R^* / \bar{M}^* C^*_{p,\infty} \qquad (6)$$

where

$$\epsilon = \left[\frac{\mu^*_{\text{ref}}}{\rho^*_\infty U^*_\infty R^*_N}\right]^{1/2} \qquad H \equiv h + \frac{u^2}{2}$$

$$\tilde{C}_l = \sum_{i=1}^{N} \delta_{il}\frac{M^*_l}{M^*_i} C_i$$

$$\Phi = \frac{\mu}{N_{Pr}}\left[\frac{\partial H}{\partial n} + (N_{Le}-1)\sum_{i=1}^{N} h_i \frac{\partial C_i}{\partial n} + (\mathrm{N_{Pr}}-1)\mathrm{u}\frac{\partial u}{\partial n} - \frac{N_{Pr}\kappa u^2}{1+n\kappa}\right] \qquad (7)$$

and Q is the divergence of the radiative flux.

Boundary Conditions

The boundary conditions at the shock are calculated by using the Rankine-Hugoniot relations. At the wall, the no-slip and no-temperature-jump boundary conditions are used; consequently, $u_w = 0$. The wall temperature and mass injection rate are either specified or calculated. For the calculated conditions, the mass injection rate is determined from an energy balance at the flowfield ablator interface. The expression for the coupled mass injection rate is

$$\dot{m} = \left(\frac{-q^*_{c,w} - q^*_{r,w}}{\Delta H^*_a}\right)\left(\frac{1}{\rho^*_\infty U^*_\infty}\right) \qquad (8)$$

The ablation process is assumed to be quasi-steady and the surface temperature is the sublimation temperature of the ablator char. The equations used for the heat of ablation and the sublimation temperatures for a phenolic-nylon ablator are the least-squares fits[6]

$$T^*_{\text{sub}} = 3450.4 + 187.0\log p^* + 9.715(\log p^*)^2, \text{ K} \qquad (9)$$

$$\Delta H^*_a + 21.334 - 2.668\log p^* + 0.766(\log p^*)^2, \text{ MJ/kg} \qquad (10)$$

where p^* is the wall pressure in atmospheres. These equations are applicable for surface pressures of 0.01 to 1.0 atm. The coupled mass injection rate and surface temperature are calculated by iterating the solution of the governing flowfield equations. and the boundary conditions.

For ablation injection, the elemental concentrations at the wall are governed by convection and diffusion are given by the equation

$$\left(\frac{\partial \tilde{C}_l}{\partial n}\right)_w - \frac{1}{\epsilon^2}\left(\frac{\dot{m}N_{Sc}}{\mu}\right)_w\left[\left(\tilde{C}_l\right)_w - \left(\tilde{C}_l\right)_-\right] = 0 \qquad (11)$$

For the radiation transport calculations, the bow shock is considered transparent and the freestream cold and transparent. The next radiative flux can be represented as the difference of two components

$$q_r = q_r^{(+)} - q_r^{(-)} \tag{12}$$

At the wall

$$q_{r,w}^{(+)^*} = \epsilon\sigma^* T^{*4} \tag{13}$$

where the emissivity, ϵ, is assumed to be 0.8. The energy reradiated from the surface is neglected in the radiation transport calculation; however, it is included in the surface energy balance [Eq. (8)].

The heat transferred to the wall due to conduction and diffusion is

$$-q_{c,w} = \epsilon^2 \left(K\frac{\partial T}{\partial n} + \frac{\mu}{N_{Sc}} \sum_{i=1}^{N} h_i \frac{\partial C_i}{\partial n} \right)_w \tag{14}$$

Radiative transport

The radiative flux, q_r, and the divergence of the radiative flux, Q, are calculated with the radiation transport model LRAD-3, as presented in Ref. 6. The radiation transport model is an extended version of a coupled line and continuum model that was originally developed by Wilson.[2] The LRAD-3 radiation model accounts for the effects of nongray self-absorption, radiative cooling, and the contribution of atomic line radiation. Twelve continuum frequency bands and nine line bands are used. The species considered for determining the radiation transport are: C, H, N, and O for both continuum and lines and CO, C_2, C_3, O_2, N_2, H_2, C_2H, and e^- for continuum. Details of the radiation transport analysis are given in Ref. 6 and are not reproduced herein.

Thermodynamic and Transport Properties

The equilibrium composition is determined by a free-energy minimization calculation as developed in Ref. 13. Thermodynamic properties for specific heat, enthalpy, and free energy and transport properties for viscosity and thermal conductivity are required for each species considered. Values for the thermodynamic[14] and transport properties[5] are obtained by using polynomial curve fits. The mixture viscosity and thermal conductivity are obtained by using the semiempirical formulas of Wilke (from Ref. 15). In this study, the binary diffusion coefficient, which is used to calculate the binary Lewis number, is set equal to the diffusion coefficient for atomic carbon diffusing into atomic nitrogen.

Air is treated as a mixture of seven chemical species, O, O_2, O^+, N, N_2, N^+, and e^-. For ablation injection, 20 chemical species are used: the seven used for air plus

$$C, C_2, C_3, CO, CN, C_2H,$$

$$C_3H, C_4H, C_2H_2, C^+, H, H_2, \text{and } HCN.$$

Method of Solution

Davis[10] presented a method for solving the viscous-shock-layer equations for stagnation and downstream flow. Moss[11,12] applied this method of solution to reacting multicomponent mixtures. The present method of solution is identical to that of Refs. 11 and 12 and, therefore, is not presented.

Results and Discussion

Results are presented for two sets of Earth entry conditions to demonstrate the important features of the present analysis. Results for both air and ablation injection are presented. Mass injection rates, $\dot{m}$, from 0 to 0.60 are considered.

Table 1 Summary of stagnation results

Case number	$\dot{m}$	Injectant	n_s^*, m	$-q_{c,w}^*$, MW/m^2	$q_{r,w}^{*(-)}$, MW/m^2
		Conditions I[a]			
1	0.00	---	0.099	4.39	45.90
2	0.05	Air	0.111	0.62	42.70
3	0.10	Air	0.120	0.14	41.60
4	0.20	Air	0.135	0.03	40.00
5	0.40	Air	0.167	0.01	37.90
6	0.05	Carbon-phenolic	0.112	0.66	32.60
7	0.10	Carbon-phenolic	0.123	0.15	29.00
8	0.20	Carbon-phenolic	0.137	0.04	27.60
9	0.40	Carbon-phenolic	0.165	0.00	27.30
		Conditions II[b]			
10	0.00	---	0.012	13.61	23.95
11	0.12	Air	0.014	1.13	20.10
12	0.12	Phenolic-nylon	0.015	0.32	15.81
13	0.30	Phenolic-nylon	0.019	0.04	13.61
14	0.60	Phenolic-nylon	0.025	0.00	13.11

[a]Conditions I: Alt = 60.96 km; $U_\infty^* = 15.24$ km/sc; $R_N^* = 3.05$ m.
[b]Conditions II: Alt = 62.2 km; $U_\infty^* = 15.24$ km/sc; $R_N^* = 0.305$ m.

Table 1 presents a summary of the flow conditions and stagnation results (shock stand-off and convective and radiative heating rates) for each of the 14 cases considered in the present study. Note that the two sets of entry conditions are considered. Conditions I are those that have been extensively studied by previous investigators[3,4,7] while Conditions II are approximately the same as Conditions I except for a much smaller nose radius.

Figures 2-7 present stagnation results for reentry Conditions I. For these conditions, the freestream Reynolds number is 0.78×10^6 and the shock temperature and pressure are 14,850K and 0.59 atm, respectively. The wall temperature (3600 K) and mass injection rates are specific. The elemental mass fractions of the carbon-phenolic ablator are: 0.049 oxygen, 0.009 nitrogen, 0.920 carbon, and 0.022 hydrogen.

Figure 2 shows the wall radiant heat flux calculated with this analysis compared to that calculated with other analyses. Results for both air and carbon-phenolic injection are shown. Note that the various analyses differ siginficantly as to the magnitude of the wall radiant heat flux. This is true for all injection rates and for both air and carbon-phenolic injection. The differences in predicted heating are due in part to differences in the radiation model. In addition, appreciable differences exist in the details of the analyses and the solution procedures. Overall, the results of this analysis are in closest agreement with those reported in Ref. 7.

The results presented in Fig. 2 are in agreement with those of previous analyses[1-7] in that carbon-phenolic injection is much more effective than air injection in reducing the wall radiant heating rate. For an injection rate of 0.2, the radiative heating is reduced 40% with carbon-phenolic injection and only 13% with air injection. For carbon-phenolic injection rates in excess of 0.2 (Table 1), additional reductions in wall radiative heating are negligible because most of the incident energy is in the optically thin region of the spectrum (see Fig. 3c).

The reason that carbon-phenolic is so much more effective than air injection in reducing the wall radiative flux is evident in Fig. 3. Figure 3 shows the spectral distrubition for both line and continuum radiation flux at the wall. Figures 3b and 3c show the wall spectral flux distribution for air and carbon-phenolic injection ($\dot{m} = 0.2$), respectively. For air injection, the continuum and line radiation are reduced to 24% and 0%, respectively, with respect to the no-injection values. For carbon-phenolic injection, the continuum and line radiation are reduced 34% and 47%, respectively, with respect to the no-injection values. When the results in Figs. 3b and 3c are compared with Fig. 3a, it is seen that the line and continuum

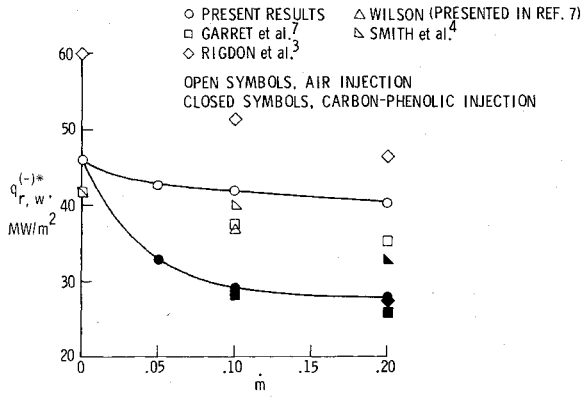

Fig. 2 Comparison of stagnation radiative heat fluxes (Conditions I).

reductions occur at photon energies in excess of 5 eV. Indeed, most of the radiant energy in excess of 5 eV is absorbed by the carbon-phenolic species for an $\dot{m}$ of 0.2.

Mass injection also has a significant effect on the flowfield profile values as shown in Fig. 4. The tangential velocity profiles (Fig. 4a) are very much dependent on the magnitude of the injection rate, but essentially, independent of whether the injectant is air or carbon-phenolic species.

The temperature profiles (Fig. 4b) are very much dependent on both the composition of the injectant and the injection rate. The profiles with carbon-phenolic injection have consistently larger gradients within the shock layer than the corresponding profiles with air injection. This occurs because of two effects. First, the specific heat of the carbon-phenolic species is greater than that for the air species; consequently, the temperature of the shock layer near the wall is lower with carbon-phenolic injection. Second, the carbon-phenolic species are much more effective than air in absorbing the radiant energy directed toward the wall. Consequently, there exists a region within the shock layer where, even though most of the composition is that of the carbon-phenolic species (see Fig. 4c), the temperature and specific heat is greater than that for the corresponding air injection rate. The combination of the strong radiation absorption in the shock layer and the increased heat capacity adjacent to the wall results in the larger temperature gradients.

The dependence of the temperature profiles on the chemical composition of the injectant is reflected in the enthalpy profiles shown in Fig. 4c. For carbon-phenolic injection, the enthalpy profiles experience a bulge or overshoot for each injection rate considered. The shape of the enthalpy profiles for carbon-phenolic injection is substantially different from that previous reported.[7] The bulge is attributed to the radiation absorption in the shock layer as will be discussed in more detail.

Figure 4 d shows how the radiation flux across the shock layer is influenced by injection rate and the composition of the injectant. Positive flux values indicate net radiant heat flux away from the wall while negative values indicate heat flux toward the wall. The present results show that the radiant flux through the shock is influenced only moderately by both the injection rate and the composition of the injectant. This is in marked contrast with the radiant flux to the wall which is strongly dependent on both the magnitude of the injection rate and the composition of the injectant.

The fraction of the shock layer for which carbon-phenolic species are present for each injection rate are shown in Fig. 4e.

Consideration of the previously discussed flowfield profile quantities shows that large gradients exist in the shock layer, particularly with carbon-phenolic injection. Therefore, to obtain accurate flowfield solutions, it is essential that the nodal spacing be made small wherever such large gradients occur. This can be accomplished by using a variable grid spacing as was done in this analysis.

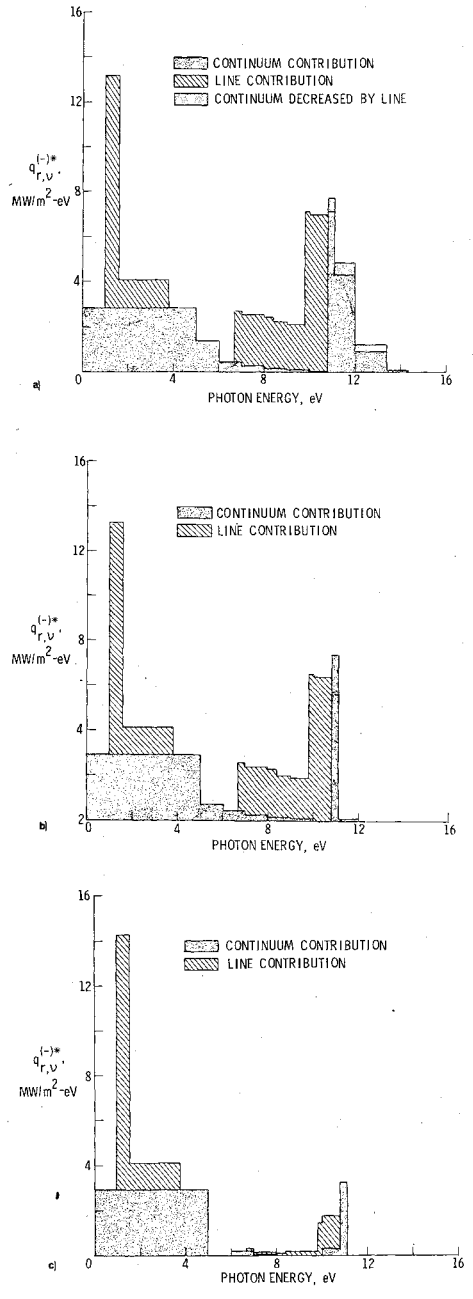

Fig. 3 Spectral distribution of radiant heat flux to the wall (Conditions I): a) $\dot{m}=0$; b) $\dot{m}=0.2$ air; c) $\dot{m}=0.2$ carbon phenolic.

The problem of numerical instability for large injection rates is characteristic of most, if not all, analyses that have been developed. For example, a converged solution of the energy equation was not obtained with the analysis of Ref. 7 for a carbon-phenolic injection rate of 0.2. The conclusion presented in Ref. 7 was that a blowing rate of 0.2 was near the stability limit for the finite-difference solution technique employed. However, with this analysis, which also uses a finite-difference solution technique, a converged solution is obtained for the 0.2 injection rate. In fact, results for injection rates twice those previously reported for Conditions I are presented in Table 1.

Additional results to substantiate the shape of the enthalpy profiles are presented in Figs. 5-7 for a carbon-phenolic injection rate of 0.2 (Case 8). Fig. 5 shows many of the profile quantities for Case 8. The bulge in the enthalpy profile is seen to occur where the chemical composition experiences a transition from air to ablation species, as indicated by the ablation mass fraction profile. The profile for the divergence of the radiative flux, Q^*, shows that the location of maximum

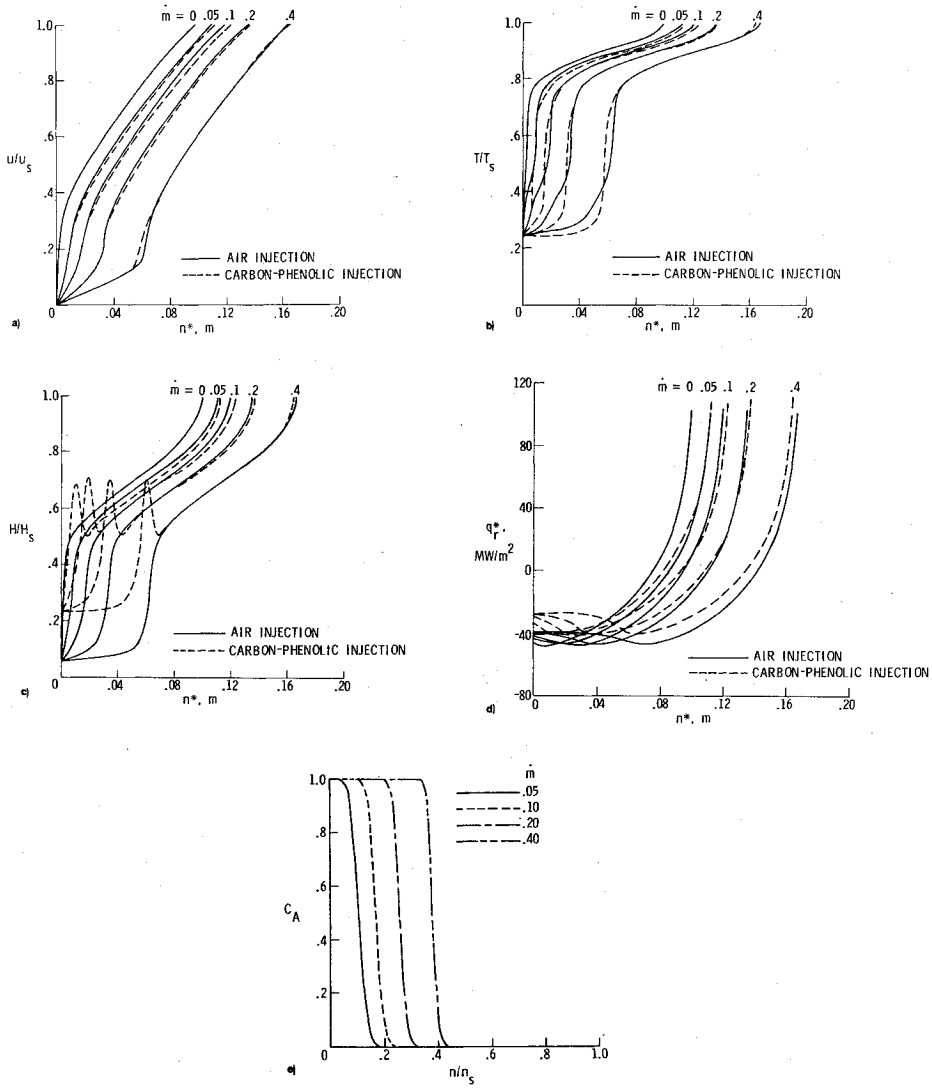

Fig. 4 Effect of mass injection on stagnation flowfield profiles (Conditions I): a) tangential velocity; b) temperature; c) enthalpy; d) radiative flux; e) ablation mass fractions.

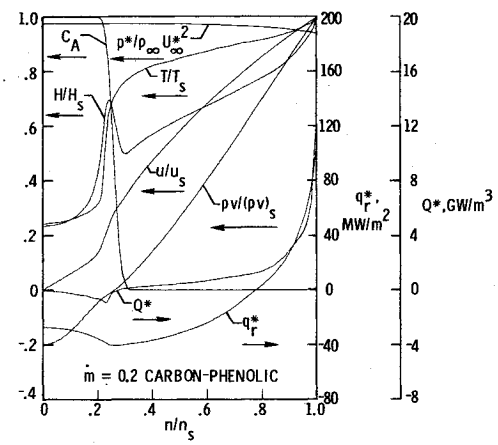

Fig. 5 Stagnation profile quantities for Case 8.

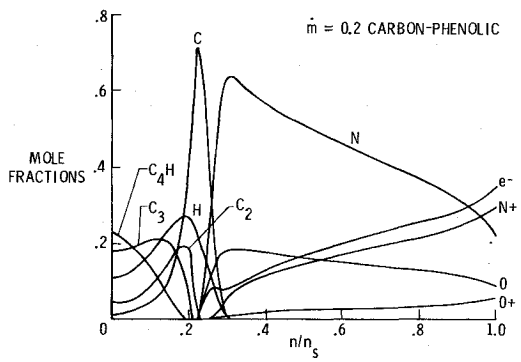

Fig. 6 Mole fraction profiles for major species (Case 8).

radiative absorption (indicated by negative Q^*) coincides with the location of the enthalpy bulge.

The mole fraction profiles for the major species are shown in Fig. 6. Both the transition from air to ablation species and the maximum concentration of the neutral carbon species occur within the spatial interval where the enthalpy bulge occurs. As resported in Refs. 1 and 2, the neutral carbon species are very effective in blocking the radiant flux toward the wall. The blocking effect is shown in Fig. 7 where the net radiative flux is shown as two components: the flux toward the shock, $q_r^{(+)^*}$, and the flux toward the wall, $q_r^{(-)^*}$. Comparisons of these profile quantities for air and carbon-phenolic injection are shown. The results show that the radiation flux toward the wall is reduced much more for carbon-phenolic injection than for air injection. This is particularly true for the shock spatial interval of 0.2 to 0.28; the same spatial interval where the enthalpy bulge occurs.

The solutions for Conditions I demonstrate that this analysis can be used to obtain detailed shock-layer quantities

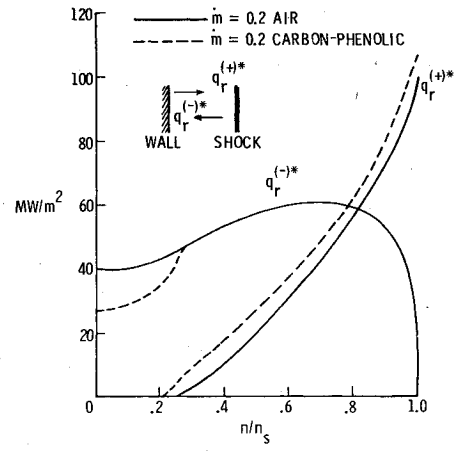

Fig. 7 Effect of injectant on radiant flux components (Conditions I).

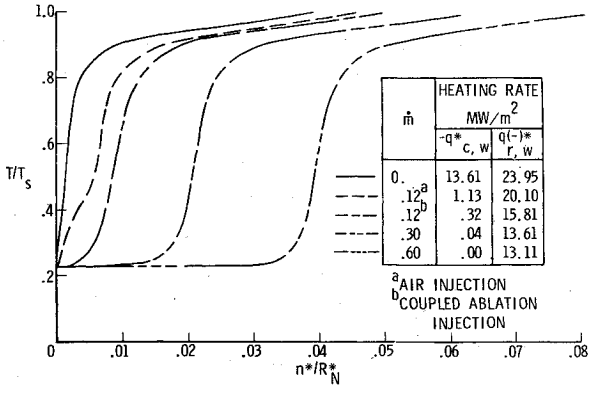

Fig. 8 Stagnation temperature profiles (Conditions II).

for large levels of injection. Downstream solutions for Conditions I were not attempted in this study. Nevertheless, a subsequent study,[16] that used the viscous-shock-layer analysis, considered downstream solutions for freestream conditions that are currently of more interest than those of Conditions I. The freestream conditions were those for Jovian entry where the freestream Reynolds number, radiative heating, and mass injection are larger than the corresponding values for Conditions I. However, numerical difficulties were encountered[16] for downstream solutions with large body half angles and large blowing. To obtain solutions for such conditions with the viscous-shock-layer approach, it may be necessary to make approximations such as the thin-shock-layer approximation as used in Ref. 16 or additional approximations.

Results are presented for Conditions II in Figs. 8-9. The body is a hyperboloid with a total included angle of 120° and a nose radius of 0.305 m. Since the nose radius is one-tenth that for Conditions I, the radiative heating is less and the convective heating greater than that for Conditions I. For Conditions II, the freestream Reynolds number is 67,850 and the stagnation shock temperature and pressure are 14,700 K and 0.5 atm, respectively. Results for both air and phenolic-nylon injection are presented. The elemental mass fractions for the phenolic-nylon ablator are: 0.15 oxygen, 0.05 nitrogen, 0.73 carbon, and 0.07 hydrogen. The stagnation wall temperature is 3395 K.

Figure 8 shows the effect of mass injection on stagnation temperature profiles. Both coupled and arbitrary injection are considered. The injection rate of 0.12 is the coupled mass injection rate for a phenolic nylon ablator. At this point in the trajectory, the mass injection is sufficient to cause a 98% reduction in $q^*_{c,w}$ and a 34% reduction in $q^{(-)*}_{r,w}$. For phenolic-nylon injection rates in excess of the coupled injection value, only small additional reductions in heating occur.

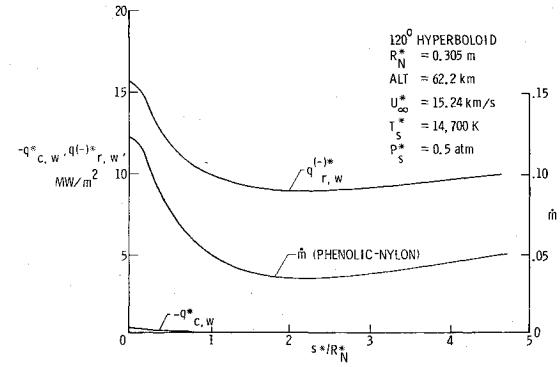

Fig. 9 Shock-layer results with coupled ablation injection.

Fig. 9 presents the wall heating rate and mass injection distributions where the mass injection from a phenolic-nylon ablator is coupled with the radiating flowfield solution. The wall temperature resulting from the coupled injection calculation is within 1% of the stagnation value. For the body shape considered and because the shock thickens with distance downstream, the radiative heating and mass injection do not continue to decrease with increasing distance downstream. Also note that the downstream mass injection is of such a magnitude that the convective heating is negligible.

Conclusions

Results are presented for Earth entry conditions that demonstrate important features of a viscous-shock-layer analysis for investigating high-energy viscous flowfields with radiation transfer. This analysis is unique in that direct solutions for large levels of mass injection can be obtained for both stagnation and downstream flows. With this analysis, a capability exists for studying flowfields where the boundary layer is blown off the surface.

The present results show that, whereas ablation injection rates up to 0.2 cause large reductions in radiative flux to the wall, injection rates greater than about 0.2 affect only small additional reductions in surface heating. It is also shown that the absorption of radiation by injected ablation species can significantly alter the shape of the enthalpy profiles. The radiation absorption can cause a bulge in the enthalpy profiles. This behavior has not been previously reported.

The downstream results with coupled phenolic-nylon injection show that, for bodies with large included angles, the radiative flux to the wall and the mass injection rate have minimum values at some point downstream. Farther downstream, the increase in shock thickness causes increases in the radiative flux and in the mass injection rate.

References

[1]Wilson, K. H. and Hoshizaki, H., "Effect of Ablation Product Adsorption and Line Transitions on Shock Layer Radiative Transport," NASA CR-1264, 1969.

[2]Wilson, K. H., "Stagnation Point Analysis of Coupled Viscous-Radiating Flow With Massive Blowing," NASA CR-1548, 1970.

[3]Rigdon, W. S., Dirling, R. B., Jr., and Thomas M., "Stagnation Point Heat Transfer During Hypervelocity Atmospheric Entry," NASA CR-1462, 1970.

[4]Smith, G. L., Suttles, J. T., Sullivan, E. M., and Graves, R. A., Jr., "Viscous Radiating Flow Field on an Ablating Body," AIAA Paper 70-218, N.Y.C., Jan. 1970.

[5]Esch, D. D., Pike, R. W., Engel, C. D., Farmer. R. C., and Balhoff, J. F., "Stagnation Region Heating of a Phenolic-Nylon Ablator During Return from Planetary Missions," NASA CR-112026, 1971.

[6]Engel, C. D., Farmer, R. C., and Pike, R. W., "Ablation and Radiation Copuled Viscous Hypersonic Shock Layers," NASA CR-112306, 1971.

[7]Garrett, L. B., Smith, G. L., and Perkins, J. N., "An Implicit Finite-Difference Solution to the Viscous Shock Layer Including the Effects of Radiation and Strong Blowing," NASA TR R-388, 1972.

[8]Sutton, K., "Coupled Nongray Radiating Flow About Planetary Entry Bodies," *AIAA Journal,* Vol. 12, Aug. 1974, pp. 1099-1105.

[9]Chou, Y. S., "Effect of Downstream Massive Blowing on Jovian Entry Heating," AIAA Paper 73-717, Plam Springs, Calif., July 1973.

[10]Davis, R. T., "Numerical Solution of the Hypersonic Viscous Shock-Layer Equations," *AIAA Journal,* Vol. 8, May 1970, pp. 843-851.

[11]Moss, J. N., "Solutions for Reacting and Nonreacting Viscous Shock Layers with Multicomponent Diffusion and Mass Injection," Ph.D. Thesis, Virginia Polytechnic Institute and State University, 1971.

[12]Moss, J. N., "Reacting Viscous Shock-Layer Solutions With Multicomponent Diffusion and Mass Injection," NASA TR R-411, 1974.

[13]Stroud, C. W., and Brinkley, K. L., "Chemical Equilibrium of Ablation Materials Including Condensed Species," NASA TN D-5391, 1969.

[14]Esch, D. D., Siripong, A., and Pike, R. W., "Thermodynamic Properties in Polynomial Form for Carbon, Hydrogen, Nitrogen, and Oxygen Systems From 500 to 15000° *K*," NASA CR-111989, 1970.

[15]Bird, R. B., Stewart, W. E., and Lightfoot, E. N., *Transport Phenomena,* Wiley, N. Y., 1960.

[16]Moss, J. N., Anderson, E. C., and Bolz, C. W., "Viscous-Shock-Layer Solutions With Radiation and Ablation Injection for Jovian Entry," AIAA Paper 75-671, Denver, Colo., May 1975.